



**Michigan
Technological
University**

Michigan Technological University
Digital Commons @ Michigan Tech

Michigan Tech Publications

3-16-2022

Ultrahigh Piezoelectric Performance through Synergistic Compositional and Microstructural Engineering

Yongke Yan
Pennsylvania State University

L. D. Geng
Michigan Technological University, liweig@mtu.edu

Li Feng Zhu
Pennsylvania State University

Haoyang Leng
Pennsylvania State University

Xiaotian Li
Pennsylvania State University

See next page for additional authors

Follow this and additional works at: <https://digitalcommons.mtu.edu/michigantech-p>



Part of the [Materials Science and Engineering Commons](#)

Recommended Citation

Yan, Y., Geng, L., Zhu, L., Leng, H., Li, X., Liu, H., Lin, D., Wang, K., Wang, Y., & Priya, S. (2022). Ultrahigh Piezoelectric Performance through Synergistic Compositional and Microstructural Engineering. *Advanced Science*. <http://doi.org/10.1002/adv.202105715>

Retrieved from: <https://digitalcommons.mtu.edu/michigantech-p/15881>

Follow this and additional works at: <https://digitalcommons.mtu.edu/michigantech-p>



Part of the [Materials Science and Engineering Commons](#)

Authors

Yongke Yan, L. D. Geng, Li Feng Zhu, Haoyang Leng, Xiaotian Li, Hairui Liu, Dabin Lin, Ke Wang, Yu Wang, and Shashank Priya

Ultrahigh Piezoelectric Performance through Synergistic Compositional and Microstructural Engineering

Yongke Yan,* Liwei D. Geng,* Li-Feng Zhu, Haoyang Leng, Xiaotian Li, Hairui Liu, Dabin Lin, Ke Wang, Yu U. Wang,* and Shashank Priya*

Piezoelectric materials enable the conversion of mechanical energy into electrical energy and vice-versa. Ultrahigh piezoelectricity has been only observed in single crystals. Realization of piezoelectric ceramics with longitudinal piezoelectric constant (d_{33}) close to 2000 pC N⁻¹, which combines single crystal-like high properties and ceramic-like cost effectiveness, large-scale manufacturing, and machinability will be a milestone in advancement of piezoelectric ceramic materials. Here, guided by phenomenological models and phase-field simulations that provide conditions for flattening the energy landscape of polarization, a synergistic design strategy is demonstrated that exploits compositionally driven local structural heterogeneity and microstructural grain orientation/texturing to provide record piezoelectricity in ceramics. This strategy is demonstrated on [001]_{PC}-textured and Eu³⁺-doped Pb(Mg_{1/3}Nb_{2/3})O₃-PbTiO₃ (PMN-PT) ceramics that exhibit the highest piezoelectric coefficient (small-signal d_{33} of up to 1950 pC N⁻¹ and large-signal d_{33} of ≈ 2100 pm V⁻¹) among all the reported piezoelectric ceramics. Extensive characterization conducted using high-resolution microscopy and diffraction techniques in conjunction with the computational models reveals the underlying mechanisms governing the piezoelectric performance. Further, the impact of losses on the electromechanical coupling is identified, which plays major role in suppressing the percentage of piezoelectricity enhancement, and the fundamental understanding of loss in this study sheds light on further enhancement of piezoelectricity. These results on cost-effective and record performance piezoelectric ceramics will launch a new generation of piezoelectric applications.


1. Introduction

Piezoelectric ceramic materials with high piezoelectric constant can generate large strain in response to applied electric field or generate high voltage in response to applied mechanical stress. Piezoelectric ceramics find application in variety of electronic, communication, imaging, sensing and electromechanical systems.^[1-3] High energy density and ease of miniaturization are further driving the development of new piezoelectric technologies, such as energy harvesters for the Internet of Things (IoT) devices.^[3] Among all the known piezoelectric materials, perovskite ferroelectrics exhibit the highest longitudinal piezoelectric strain/charge coefficient, d_{33} . In perovskite ferroelectrics, the longitudinal piezoelectric coefficient d_{33} can be expressed as $d_{33} = 2Q_{33}P_r\epsilon_{33}$, where Q_{33} is the electrostrictive coefficient, P_r is the remanent polarization, and ϵ_{33} is the dielectric permittivity.^[4,5] The most widely adopted approach for enhancing the piezoelectric response d_{33} is by increasing the dielectric permittivity ϵ_{33} via flattening of the Gibbs free energy landscape with respect to the polarization (lowering the energy barrier for ferroelectric polarization rotation). The traditional method to flatten energy landscape is by designing composition-induced multiphase region, such as morphotropic phase boundary

Y. Yan, L.-F. Zhu, H. Leng, X. Li, H. Liu, S. Priya
Department of Materials Science and Engineering
Pennsylvania State University
University Park, PA 16802, USA
E-mail: yxy355@psu.edu; sup103@psu.edu

L. D. Geng, Y. U. Wang
Department of Materials Science and Engineering
Michigan Technological University
Houghton, MI 49931, USA
E-mail: liweig@mtu.edu wangyu@mtu.edu

D. Lin, K. Wang
Materials Research Institute
Pennsylvania State University
University Park, PA 16802, USA

 The ORCID identification number(s) for the author(s) of this article can be found under <https://doi.org/10.1002/adv.202105715>

© 2022 The Authors. Advanced Science published by Wiley-VCH GmbH. This is an open access article under the terms of the Creative Commons Attribution License, which permits use, distribution and reproduction in any medium, provided the original work is properly cited.

DOI: 10.1002/adv.202105715

(MPB) or polymorphic phase transition (PPT).^[6,7] There are two emerging approaches to further improve the piezoelectric response, namely, compositional local structural heterogeneity and microstructural texture engineering.

The approach of compositional local structural heterogeneity engineering is to create heterogenous polar nanoregions by means of either nanoscale B-site cation ordering (for example, Mg²⁺ and Nb⁵⁺ short range ordering in PMN) or A-site aliovalent doping (such as, Sm³⁺ doped PMN-PT, and La³⁺ doped Pb(Zr,Ti)O₃, PLZT), and hence introduce interfacial energies associated with local polarization and strain discontinuities.^[5,8–13] The competition between the matrix energy and the interfacial energies can flatten the energy landscape to increase the dielectric permittivity and piezoelectricity.^[12] The approach of local structural heterogeneity engineering has been demonstrated in recent breakthrough in Sm³⁺-doped Pb(Mg_{1/3}Nb_{2/3})O₃-PbTiO₃ (PMN-PT) materials which exhibit ultrahigh longitudinal piezoelectric coefficients d_{33} of ≈ 1500 pC N⁻¹ in ceramics.^[12] The introduction of Sm³⁺ dopant on the A-site of PMN-PT lattice created local structural heterogeneity and disruptions in the long-range ferroelectric domains, resulting in significant increase in both dielectric permittivity and piezoelectric response.^[12,13]

The approach of microstructural texture engineering in ceramics is to utilize the strong intrinsic anisotropy of piezoelectric properties available in single crystals. For example, the d_{33} of up to 2820 pC N⁻¹ in [001]_{PC}-oriented rhombohedral PMN-PT single crystals is nearly 15 times larger than the d_{33} -value (190 pC N⁻¹) along <111>_{PC} direction.^[14] Since the practical application of single crystals is challenged by their relatively higher cost, time-consuming synthesis process, and composition inhomogeneity due to incongruent melting issues, the most widely used piezoelectric materials are based on polycrystalline ceramics with random grain orientations exhibiting average piezoelectric properties. Considering the beneficial characteristic of anisotropy in polycrystalline materials, extensive efforts have been made toward developing crystallographic textured polycrystalline ceramics, referring to ceramics with large degree of grains oriented along a preferred crystallographic direction. A wide variety of textured piezoelectric ceramics have been reported with enhanced piezoelectric properties^[7,15–22]. For example, the longitudinal piezoelectric coefficient, d_{33} , of [001]_{PC} textured PMN-PT and PMN-PZT ceramics was found to exceed 1000 pC N⁻¹, which is about two to five times higher than that of the random ceramics.^[15,16]

The aforementioned compositional local structural heterogeneity and microstructural texture engineering have been individually studied and much progress has been made based on these strategies. However, it has been challenging to implement the synergistic design that exploits both these mechanism in the same material. One of the main challenges in achieving this synergistic approach is that microstructural design is significantly influenced by composition induced local structural heterogeneity. This mutual coupling presents resistance in obtaining the desired local structure and microstructure. Here, we demonstrate for the first-time success in resolving this challenge which resulted in record piezoelectric performance in ceramics.

2. Results and Discussion

2.1. Synergistic Design Strategy for Ultrahigh Piezoelectricity in Ceramics

Guided by phenomenological models and phase-field simulations, we propose a synergistic approach of local structural heterogeneity and grain texturing to enhance piezoelectricity via flattening the energy landscape of polarization. Local structural heterogeneity was introduced by doping rare-earth elements in classical relaxor ferroelectrics, and its fraction depends on the concentration of dopants. It is complex to exactly quantify the percentage of local structural heterogeneity just by taking into account the doping amount of rare-earth elements. Rather a good understanding of the underlying physical mechanisms is needed. Therefore, to explore the doping effect on piezoelectricity, we invoked Landau theory to examine how the piezoelectric coefficient d_{33} changes with the volume fraction of local heterogeneities. **Figure 1A** illustrates the enhancement of d_{33} via the increment of heterogeneity volume fraction for PMN-PT. In this work, PMN-PT is in rhombohedral phase with the spontaneous polarization along <111> directions at room temperature. The inclusion of heterogeneity that favors the orthorhombic phase (polarization along <110> directions) can flatten the energy landscape because of the competition between bulk and interfacial energy. According to the phase-field simulation in **Figure 1B**, the coupling between matrix and heterogeneities is collinear at room temperature,^[23] where the polarization in heterogeneities is almost parallel with that in matrix to reduce the interfacial energies. Such a collinear behavior can be examined from the angle between polarization and [110]-direction. These “collinear” heterogeneities will facilitate the polarization rotation of nearby regions and result in a highly fattened energy profile, leading to increased permittivity and piezoelectricity. The detailed phase-field simulation results on the effect of heterogeneity fraction on d_{33} are shown in **Figure S1** (Supporting Information). The simulations reveal that the elevated fraction of heterogeneities can effectively increase d_{33} until reaching a critical point beyond which the heterogeneity's become dominant and d_{33} begins to drop.

Texturing can further increase the piezoelectricity of rare-earth doped PMN-PT, as illustrated in **Figure 1C,D**. The texturing technique enables grains to align with each other along a specific crystallographic orientation, which enables design of polycrystalline ceramics that outperform traditional ceramics by exhibiting piezoelectric performance comparable or even equal to that of single crystals. **Figure 1C** schematically illustrates the grain orientation distributions in random and textured polycrystals. For the random polycrystal, all the grain orientations are randomly distributed. For the [001]_{PC}-textured polycrystal, the grains are oriented along the [001]_{PC} crystallographic axis with [010]_{PC} and [100]_{PC} crystallographic axes distributed randomly. For both random and textured polycrystals, once they are poled along a certain direction (*z*-direction), the eight <111> directions become nonequivalent and the spontaneous polarizations in each grain prefers to stay as close to the poling direction as possible. Herein, *x*, *y*, and *z* are defined in the “lab coordinate” while directions labeled with square brackets are defined in the

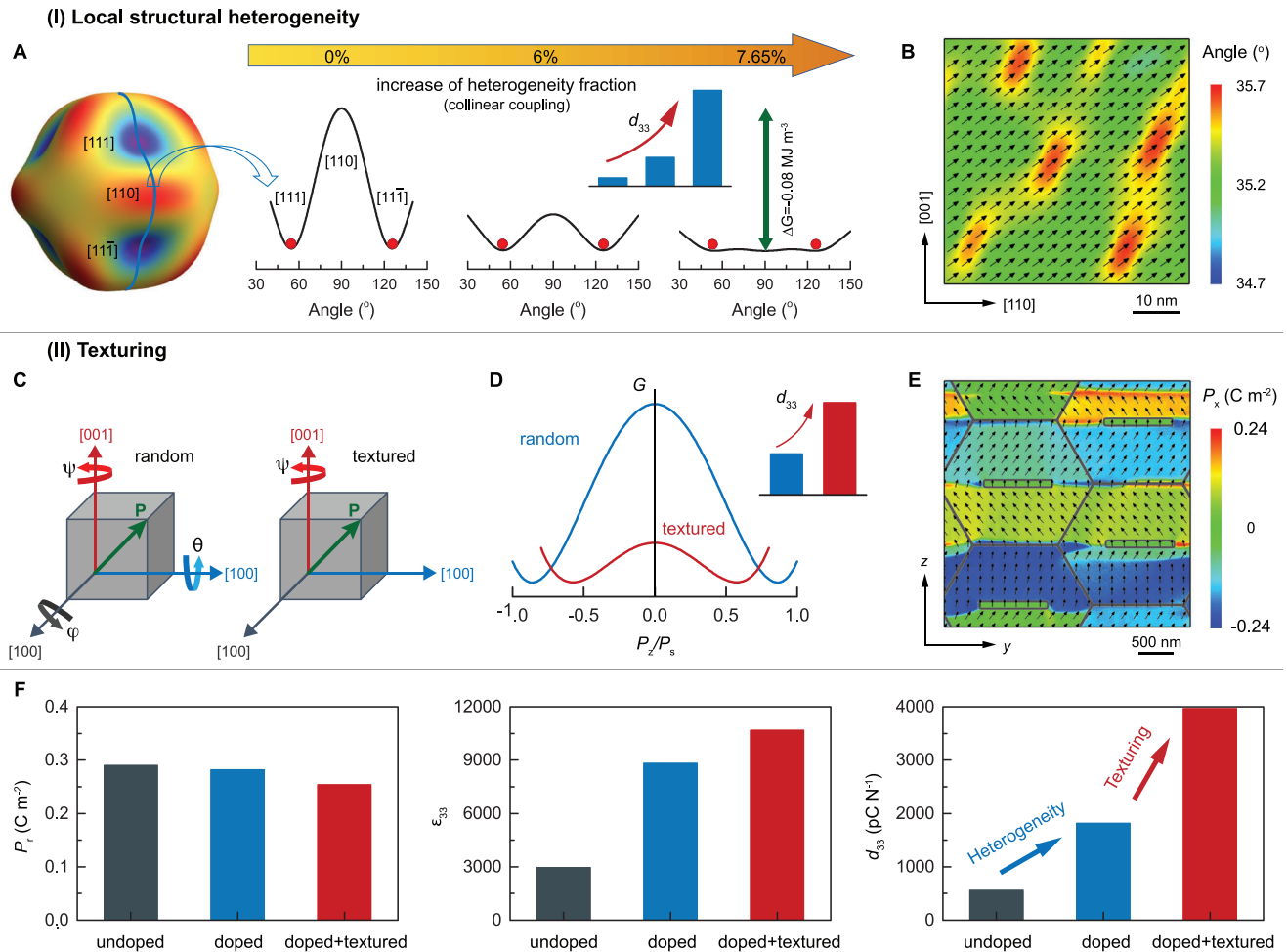


Figure 1. Phenomenological illustration and phase-field simulation of enhanced piezoelectricity via local structural heterogeneity and texture engineering. A) Landau free energy of ferroelectrics with different volume fraction of the local structural heterogeneity. B) Phase-field simulated polarization distribution of PMN-PT with 5% heterogeneities. C) Schematic diagram of grain orientation distributions in random and textured polycrystals. D) Landau free energy profiles with respect to the polarization component P_z (normalized by saturated polarization P_s) along poling direction z for random and textured polycrystals, where the inset shows the corresponding d_{33} increment. E) Phase-field simulated polarization distribution of [001]_{PC}-textured PMN-PT polycrystal with 5% heterogeneities (doped) after electrical poling along z -direction. F) Phase-field simulation of the remanent polarization P_r , dielectric permittivity ϵ_{33} , and longitudinal piezoelectric coefficient d_{33} for undoped, doped, and doped+textured polycrystals. Note: x , y , and z are defined in the “lab coordinate” while directions labeled with square brackets are defined in the “crystallographic coordinate,” and z is the poling direction that coincides with [001] for [001]_{PC}-textured polycrystal in our simulations.

“crystallographic coordinate,” and z is the poling direction that coincides with [001] for [001]_{PC}-textured polycrystal in our simulations. If neglecting the correlation between grains, the average polarization in the poling direction is $P_z/P_s = \sqrt{3}/2$ for random polycrystal and $P_z/P_s = 1/\sqrt{3}$ for [001]-textured polycrystal, as indicated by the energy-minimum points in Figure 1D. It is worth noting that the average angle between polarization and poling direction is 30° for random polycrystal and 54.74° for textured (which is the maximum allowed angle for poled rhombohedral ferroelectrics). Since the piezoelectric response for relaxor-PT crystals is related to “polarization rotation” rather than “polarization elongation,”^[24] textured polycrystal with the larger angle will exhibit a higher permittivity and piezoelectricity as compared to random polycrystal. According to the equivalent

energy profiles in Figure 1D, the latter is found to have a flatter energy landscape and thus a higher d_{33} .

To examine the synergistic design of local structural heterogeneity and texturing, we performed phase-field simulations for undoped (random polycrystal), doped (random polycrystal with heterogeneity), and doped + textured (textured polycrystal with heterogeneity) PMN-PT ceramics. As discussed above, under a poling treatment, local polarizations will be aligned along the spontaneous polarization directions that are closer to the poling direction. Figure 1E shows the simulated polarization distribution of [001]_{PC}-textured PMN-PT polycrystal with 5% heterogeneities (doped) after electrical poling along z -direction. Upon poling, there are four equivalent polarization directions for the rhombohedral phase, which form a “stripe” domain structure, in analogy to stripe domains separated by 109° domain walls

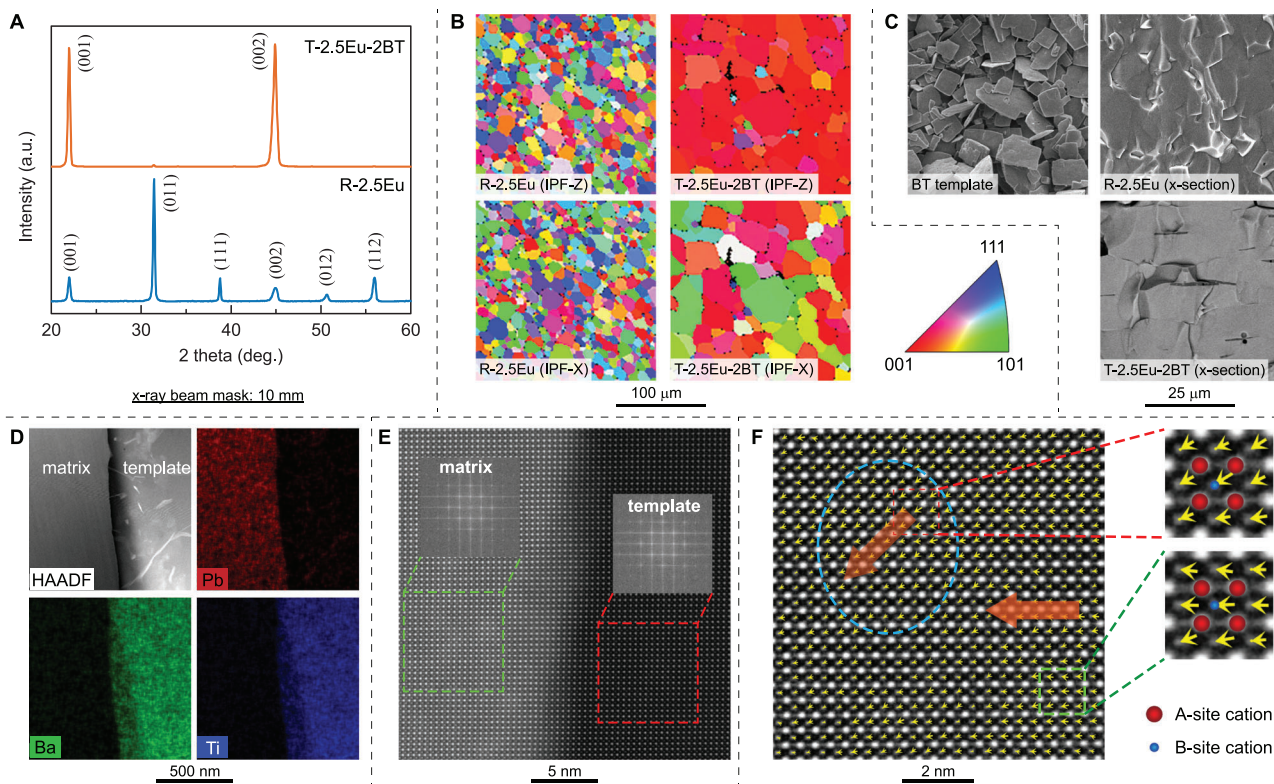


Figure 2. Multiscale microstructures of random and textured Eu^{3+} -doped PMN-PT at different scales (cm to nm). A) X-ray diffraction patterns of random and textured Eu^{3+} -doped PMN-PT ceramics, abbreviated as R-2.5Eu and T-2.5Eu-2BT, respectively. B) Inverse pole Figure (IPF) maps of R-2.5Eu and T-2.5Eu-2BT ceramics, measured by the SEM-EBSD technique. The IPF components in Z and X directions reveal the sample's out-of-plane (normal) and the in-plane spatial grain orientation distributions. C) SEM images of [001] BaTiO_3 templates and cross-sections (x-section) of R-2.5Eu and T-2.5Eu-2BT ceramics. D) Element distribution mappings of T-2.5Eu-2BT textured ceramics, measured by STEM-EDS technique. E) High resolution STEM image of template/matrix interface in T-2.5Eu-2BT textured ceramics. F) HR-STEM images of T-2.5Eu-2BT matrix recorded along the crystallographic [001]_{PC} direction. The polar vectors (arrows) are given for each unit-cell column in the atomic resolution STEM. The positions of the A-site and B-site atomic columns are indicated in the enlarged images on the right.

in single crystals. This single-crystal domain feature present in polycrystals results from the fixed [001] crystallographic axis. However, since the other axes are free and randomly distributed, the electrical and elastic correlations between neighboring grains still exist, which makes the polarizations deviate from their original directions and thus results in imperfect “stripe” domains with non-109° domain walls. Please note that such a stripe-like domain structure will not be present in random polycrystals (Figure S2, Supporting Information). The nucleation of these “stripe” domain walls usually takes place from grain boundaries as well as the tetragonal-phase BaTiO_3 templates. Figure 1F shows the simulated polarization remanence P_r , dielectric permittivity ϵ_{33} , and piezoelectric coefficient d_{33} for the three types of ceramics, undoped (random polycrystal), doped (random polycrystal with heterogeneity), and doped + textured (textured polycrystal with heterogeneity). Piezoelectric coefficient d_{33} is found to be significantly increased through the local structural heterogeneity and texture engineering. For heterogeneity engineering, the enhancement of d_{33} is mainly attributed to the increment of ϵ_{33} . For texture engineering, ϵ_{33} is increased, resulting in the enhancement of d_{33} . These findings suggest that ultrahigh piezoelectricity can be achieved in polycrystal ceramics by following the proposed synergistic design.

2.2. Multiscale Microstructures of Synthesized [001]_{PC}-Textured and Eu^{3+} -Doped PMN-PT Ceramics

To experimentally implement the proposed synergistic design, PMN-PT system is selected, as significant improvement of piezoelectricity has been demonstrated individually in rare-earth doped PMN-PT system [25] and textured PMN-PT ceramics.[15] For a better understanding of dielectric, ferroelectric and piezoelectric behavior of PMN-PT system with synergistic strategy of the heterogeneity and texturing techniques, highly [001]_{PC}-textured Eu^{3+} -doped PMN-PT piezoelectric ceramics were prepared by templated grain growth technique using [001]_{PC} BaTiO_3 templates (Eu^{3+} was added in the form of Eu_2O_3 , please refer to Materials and Methods section for synthesis details). Figure 2 depicts the microstructures of 2.5 mol% Eu^{3+} -doped and [001]_{PC}-textured PMN-28PT ceramics with 2 vol% BaTiO_3 templates on a variety of length scale from cm to nm, abbreviated as T-2.5Eu-2BT. For comparison, the random counterparts were prepared by the same processing method but without adding templates, abbreviated as R-2.5Eu. Figure 2A shows the X-ray diffraction patterns for T-2.5Eu-2BT and R-2.5Eu ceramics, respectively. Both samples exhibit perovskite phase, while textured ceramics show a remarkable enhancement in the intensity of

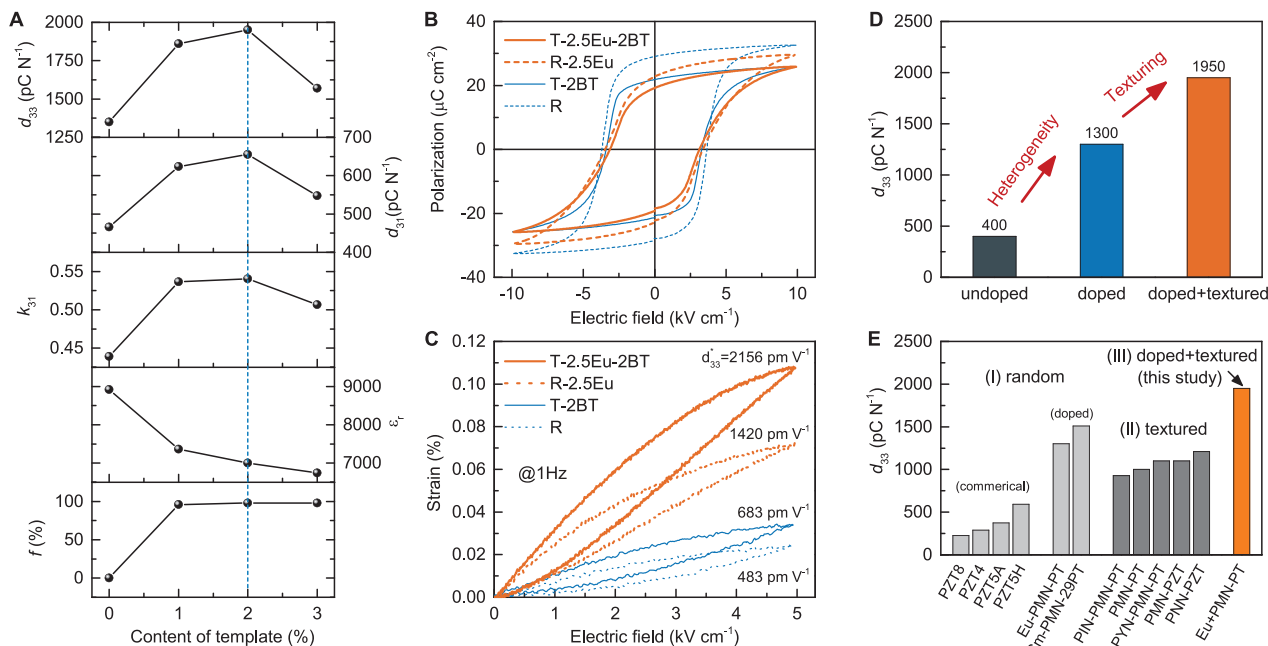


Figure 3. Piezoelectric and dielectric properties of $[001]_{PC}$ -textured and Eu^{3+} -doped PMN-PT ceramics. A) Texture degree f , dielectric constant ϵ_r , electromechanical coupling k_{31} , piezoelectric coefficient d_{31} and d_{33} of 2.5 mol% Eu^{3+} -doped PMN-PT with different contents of BaTiO_3 templates. B) Polarization-electric field loops of random PMN-PT (R), PMN-PT textured ceramics with 2 vol% BT template (T-2BT), random Eu^{3+} -doped PMN-PT (R-2.5Eu), and 2.5 mol% Eu -doped PMN-PT textured ceramics with 2 vol% BT template (T-2.5Eu-2BT), measured at 1 Hz. C) Electric-field-induced strain of R, T, R-2.5, and T-2.5Eu-2BT ceramics, measured at 1 Hz. D) Comparison of piezoelectric coefficient d_{33} between undoped (R), doped (R-2.5Eu) and doped+textured (T-2.5Eu-2BT) ceramics. E) Comparison of piezoelectric coefficient d_{33} between commercial PZT ceramics, reported lead-based textured ceramics and Eu^{3+} -doped PMN-PT textured ceramics (T-2.5Eu-2BT). References are listed in the Supporting Information.

the (001) diffraction peak compared to random ceramics. The Lotgering factor of the textured sample is over 98%, indicating a strong $[001]_{PC}$ preferred grain orientation. Electron backscatter diffraction (EBSD) was performed to further identify the crystallographic orientation of each grain in the textured sample. From Figure 2B, it can be observed that the grain orientation in random sample are randomly distributed in three-dimensions, while the $[001]_{PC}$ -oriented grains in textured sample are well aligned along the thickness direction (z , out of casting plane). Further, the $[100]_{PC}$ and $[010]_{PC}$ orientations of grains in textured samples are randomly distributed in the casting plane. This is related to the fact that unidirectional shear force was used for aligning the templates. As shown in Figure 2C, BaTiO_3 template shows a plate-like morphology, with length of 10–20 μm and thickness of 0.5–1 μm , respectively. These high-aspect-ratio BaTiO_3 platelets can be well aligned in the matrix during the tape casting via the shear force applied by doctor blade. The 2.5Eu-doped PMN-28PT matrix epitaxially grew from these aligned BaTiO_3 templates (Figure 2C), yielding strong $[001]_{PC}$ orientation out of the casting plane. Interfacial regions among BaTiO_3 template and 2.5Eu-PMN-28PT matrix were investigated by high resolution scanning transmission electron microscope (HR-STEM) and energy dispersive spectrometry (EDS) element mapping, as shown in Figure 2D,E. The sharp interface indicates a negligible inter-diffusion between template and matrix. The atomic arrangement, characterized by fast Fourier transform (FFT) diffraction patterns from HR-STEM, indicates the epitaxial growth along $[001]_{PC}$ orientation, which is the origin of textured structure. With the similar approach for identifying the local

structural heterogeneity in Sm-doped PMN-PT,^[12] the positions of the A-site and B-site atomic columns in $[001]_{PC}$ -textured and Eu^{3+} -doped PMN-PT ceramics are depicted by HR-STEM as shown in Figure 2E. According to the atomic positions in this Figure 2F, the atomic displacements are presented as vectors pointing from the center of a B-site cation to the center of its four nearest neighboring A-site cations. These atomic displacements represent the magnitudes and directions of the polar vectors for each unit-cell column. The HR-STEM images clearly reveal the existence of local structural heterogeneity at the nanoscale in $[001]_{PC}$ -textured and Eu^{3+} -doped PMN-PT ceramics.

2.3. Piezoelectricity of $[001]_{PC}$ -Textured and Eu^{3+} -Doped PMN-PT Ceramics

Figure 3A shows the dielectric and piezoelectric properties of $[001]_{PC}$ -textured 2.5Eu-PMN-PT ceramics with different amounts of BaTiO_3 templates. It can be observed that texturing degree f reaches 96% even with 1 vol% templates and slightly increases with further increasing template content. In contrast, the dielectric constant ϵ_r decreases with template content due to the low permittivity of BaTiO_3 ($\epsilon_r = 130$) along $[001]_{PC}$ direction^[26]. This phenomenon has also been observed in textured PMN-PT without Eu^{3+} doping.^[15] Piezoelectric coefficient d_{33} shows a peak value of 1950 pC N^{-1} with 2 vol% template, which is different from the monotonous change of texture degree f and dielectric constant ϵ_r . To understand this behavior, the equation for $d_{33} = 2Q_{33}P_r\epsilon_{33}$ is discussed here again. The piezoelectric

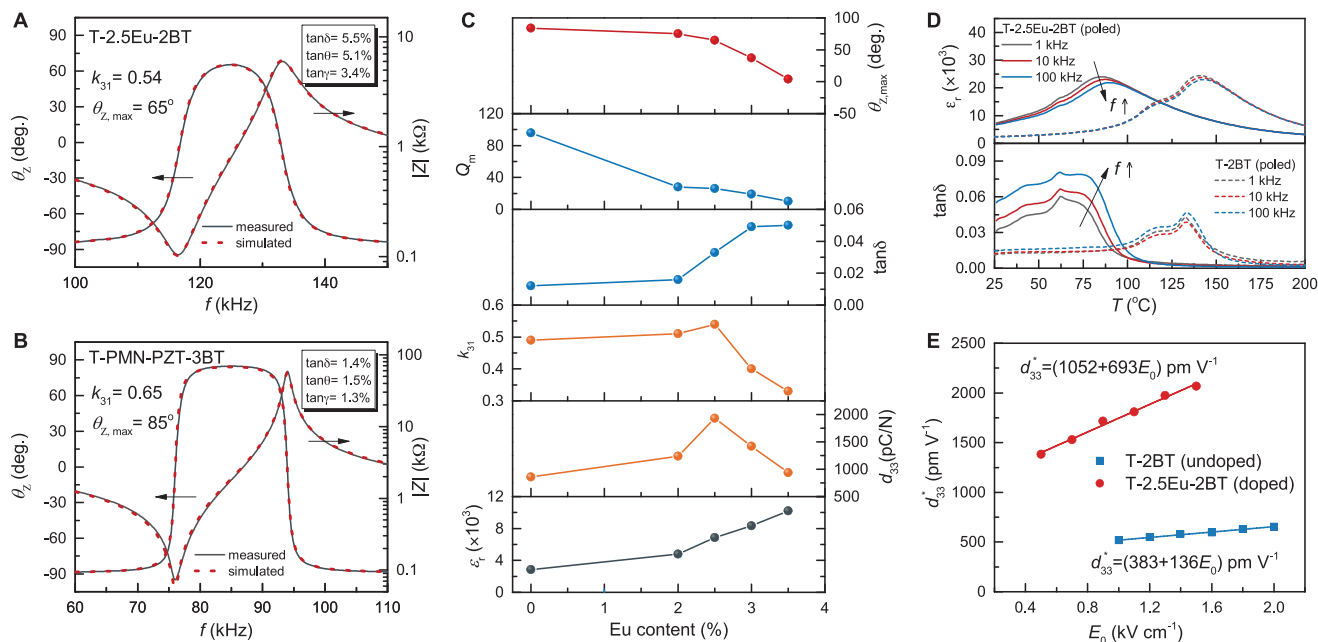


Figure 4. Losses of $[001]_{PC}$ -textured and Eu^{3+} -doped PMN-PT ceramics. Impedance $|Z|$ and impedance phase angle θ_Z spectra of A) T-2.5Eu-2BT textured ceramics and B) T-PMN-PZT-3BT textured ceramics. Here, the dielectric loss $\tan \delta$, piezoelectric loss $\tan \theta$, and electromechanical loss $\tan \gamma$ were fitted using loss incorporated equivalent circuit. C) Dielectric and piezoelectric properties of textured PMN-PT ceramics with different contents of Eu^{3+} dopant. D) Temperature-dependent dielectric constant ϵ_r and dielectric loss $\tan \delta$ of textured T-2BT and T-2.5Eu-2BT ceramics. E) Rayleigh behavior for d_{33}^* as a function of amplitude E_0 at 1 Hz.

coefficient d_{33} is strongly related to the variation of Q_{33} , P_r and ϵ_{33} . The electrostrictive coefficient Q_{33} of perovskite ferroelectrics is highly anisotropic. The maximum electrostrictive coefficient Q_{33} is along the $\langle 001 \rangle_{PC}$ directions, while the moderate and minimum values are along the $\langle 011 \rangle_{PC}$ and $\langle 111 \rangle_{PC}$ directions, respectively.^[27] It is therefore concluded that higher $[001]_{PC}$ texturing degree will generate larger Q_{33} . In regards to P_r , theoretically, the intrinsic value for the rhombohedral phase follows the relationship $P_{r,[001]_{PC}} = P_{r,\langle 111 \rangle_{PC}} / \sqrt{3}$. It can be expected that P_r decreases with the increase of $[001]_{PC}$ texturing degree in textured ceramics. This trend has been observed in this study (Figure 3B) and previous studies.^[28–30] Therefore, the opposite trend of ϵ_r and P_r , and Q_{33} change with increase in BaTiO_3 template content, provides a peak point in piezoelectric properties with 2 vol% BT template. Figure 3C shows the electric-field-induced strain for undoped/doped and random/textured ceramics, where it can be observed that both the addition of Eu^{3+} dopant and $[001]_{PC}$ texturing improves the strain and the corresponding large-signal piezoelectric coefficient d_{33}^* . Figure 3D shows the changes in small-signal d_{33} with Eu^{3+} doping and texturing, and the experimental result is consistent with the theoretical prediction as shown in Figure 1C. Through the combination of Eu^{3+} doping and texture engineering, the highest d_{33} of 1950 pC N⁻¹ is achieved. Figure 3E compares the piezoelectric coefficient d_{33} among different types of piezoelectric ceramics, including PZT ceramics,^[31] reported lead-based textured ceramics^[15,16,22,32] and Eu^{3+} -doped PMN-PT textured ceramics (T-2.5-2BT) designed in this study. From this figure, it can be observed that the Eu^{3+} -doped PMN-PT textured ceramics (T-2.5-2BT) synthesized in this study have the highest values among all the published piezoelectric ceramics.

2.4. Loss in $[001]_{PC}$ -Textured and Eu^{3+} -Doped PMN-PT Ceramics

Although the piezoelectric coefficient d_{33} of $[001]_{PC}$ -textured Eu^{3+} -doped PMN-PT (T-2.5Eu-2BT) ceramics possess the highest value among all reported piezoelectric ceramics, the percentage of piezoelectricity enhancement from texturing is only 50% (from 1300 pC N⁻¹ in R-2.5Eu to 1950 pC N⁻¹ in T-2.5Eu-2BT), which is smaller than the value expected based on the theoretical prediction (Figure 1C) and previous experimental results reported in other compositions. Experimentally, over 100% improvement has been widely achieved in a variety of compositions, such as PMN-PT, PMN-PZT,^[16] BNT-BT,^[33] KNN,^[20] BCZT,^[21] and PIN-PMN-PT.^[22] Therefore, the origin of limited enhancement of piezoelectric coefficient in highly $[001]_{PC}$ -textured and Eu^{3+} -doped PMN-PT ceramics is necessary to be investigated. There is another observation that the coupling coefficient k_{31} of textured and Eu^{3+} -doped PMN-PT ceramics is only 0.54, which is much lower than the values reported for textured PMN-PT (0.60) and textured PMN-PZT (0.65). According to the relation: $d_{31} = k_{31} \sqrt{s_{33} \epsilon_{33}}$, high k_{31} will result in high d_{31} . Since the texturing degree of textured and Eu^{3+} -doped PMN-PT is over 96%, which is similar to the values for textured PMN-PT and textured PMN-PZT, the lower k_{31} should be related to composition instead of texturing degree. As indicated by impedance spectra in Figure 4A,B, the relatively lower k_{31} in T-2.5Eu-2BT is related to the low impedance phase angle $\theta_{Z,\text{max}}$. Based upon the coupled electrical-mechanical constitutive relations at resonance, it is well-known that the impedance phase angle $\theta_{Z,\text{max}}$ is usually related to low poling degree, induced by various losses, including dielectric loss $\tan \delta$, piezoelectric loss $\tan \theta$, and electromechanical loss $\tan \gamma$.^[34–37] The impedance spectra can be

simulated using loss incorporated equivalent circuit.^[34,37] The simulation results in Figure 4A,B indicate that the T-2.5Eu-2BT exhibits much higher loss than PMN-PZT-3BT. Figure S3 (Supporting Information) simulates the effect of different types and different magnitudes of losses on the impedance phase angle. It was found that all losses, especially electromechanical loss $\tan \gamma = 1/Q_m$, have significant impact on the phase angle $\theta_{Z,max}$. To further confirm this analysis, the effect of Eu^{3+} dopant content on the dielectric, piezoelectric properties, and loss factors is investigated. As shown in Figure 4C, with the increase in Eu^{3+} content, the dielectric permittivity ϵ_r significantly increases while loss factors (dielectric loss $\tan \delta$, electromechanical loss $1/Q_m$) are also significantly increased. The increase of dielectric permittivity ϵ_r benefits the increase of piezoelectric coefficient d , while the increase of loss will reduce the impedance phase angle $\theta_{Z,max}$ and the electromechanical coupling k . This opposite trends of ϵ_r and k limit the enhancement of piezoelectric properties d .

In order to understand why the losses of PMN-PT increase significantly with the increase of Eu^{3+} dopant content, it is very important to determine the fundamental contributions to losses. Figure 4D shows the temperature dependent dielectric behavior of the textured ceramics. It can be observed that the T-2.5Eu-2BT has lower phase transition, stronger frequency dispersion of dielectric permittivity, and larger dielectric loss than undoped T-2BT, PMN-PT,^[38] and PMN-PZT (Figure S4, Supporting Information). Similar to the La^{3+} in PZT, Eu^{3+} cations occupy A-site by replacing the Pb^{2+} in PMN-PT, resulting in Pb^{2+} vacancies. In this case, Eu^{3+} as the donor dopant imparts a “soft” piezoelectric behavior (enhanced d_{33} but increased losses). The large losses include high dielectric loss due to reduced resistivity/increased leakage (Figure S5, Supporting Information) and high mechanical loss (lower mechanical quality factor Q_m as shown in Figure 4C) due to easier domain wall motion. Since the losses and piezoelectric response in ferroelectric piezoelectrics are closely related to domain wall motions,^[35,36] Rayleigh analysis was conducted to understand the effect of Eu^{3+} dopant on intrinsic and extrinsic piezoelectric response in textured ceramics. As shown in Figure 4E, the Eu^{3+} dopant not only greatly increases the intrinsic piezoresponse d_{int} from 383 pm V^{-1} to 1052 pm V^{-1} , but also significantly increases the extrinsic piezoelectric response αE_0 from 136 E_0 pm V^{-1} to 693 E_0 pm V^{-1} . The large extrinsic piezoelectric contributions resulting from the irreversible domain wall motion drive high losses and low electromechanical quality factor Q_m , as observed in Eu^{3+} doped textured ceramics. The losses in ferroelectric piezoelectric materials are strongly related to phase transition and Eu dopant as shown in Figure S7 (Supporting Information). It can be observed that the hysteresis loss reaches maximum near the phase transition temperature, and Eu dopant results in higher hysteresis loss near the room temperature.

2.5. Understanding of Loss Mechanism in Ferroelectrics

The losses in ferroelectric piezoelectric materials are strongly related to ferroelectric domain evolution, which is correlated to phase transition and heterogeneity. To understand the underly-

ing mechanisms of loss in ferroelectrics, we perform phase-field simulations to study the polarization behaviors induced by electric field at the domain level. We first investigate the temperature dependence of losses in undoped ferroelectrics and then examine the heterogeneity effect in doped ferroelectrics. Figure 5A shows the temperature-dependent polarization hysteresis induced by electric field E that is applied along [001] direction. As the temperature increases from 25 °C (room temperature) to 75 °C (around the R-T phase transition temperature), the loss is increased from 4.7% to 14.4% for undoped ferroelectrics. Generally, polarization rotation and domain wall motion are the two major mechanisms responsible for the loss in ferroelectrics, which also depends on frequency.^[39,40] Our simulations reveal that the loss is mainly contributed by domain wall motion while the polarization rotation contribution is almost negligible (at relatively low frequency), because of the faster response of polarization rotation stimulated by electric field. The position of a domain wall depends on the polarization direction which can be changed easily by electric field. Once the polarization is rotated, the domain wall energy is increased accordingly and therefore, the domain wall will adjust its position to reduce the energy. Upon the removal of electric field, the polarization can return to its original state “immediately,” but the domain wall needs more time to come back, especially for long domain walls. In fact, unless the domain wall returns to the original position, the polarization will never come back to its exact initial state, which is the origin of hysteresis. Domain wall vibrations have lower influence on determining the hysteresis as these motions are reversed immediately upon removal of the field. Figure 5C,D illustrate the domain wall motion under electric field. The domain wall angle is changed from 47.3° to 43.6° as the electric field increased from -1 to 1 kV cm^{-1} . As the temperature increases, polarization rotation becomes easier and hence the domain wall motion is enhanced, which eventually results in the highest loss at the phase transition temperature. Besides domain wall motion, the domain wall broadening also plays a role. At room temperature, the 71° domain wall is narrow, while at the phase transition temperature, the domain wall becomes broader, based on our simulation results. Figure 5C,D show the domain wall broadening induced by electric field, associated with the change of domain wall type. Since a broader domain wall can overcome pinning sites more easily, it can further enhance the domain wall motion process and thus increase the loss. Figure 5B illustrates the origin of domain wall broadening at the phase transition temperature $T_{R-T} = 73.4$ °C according to Landau theory. At the phase transition, the tetragonal (T) phase possesses the same energy as the rhombohedral (R) phase, so that it will experience a lower energy if the polarization follows Path B instead of Path A. To examine the heterogeneity effect in doped ferroelectrics, the hysteresis at 50 °C (near the R-T phase transition temperature $T_{R-T} = 48.9$ °C for PMN-PT with 5% heterogeneity) is considered, which exhibits a loss as large as 30.6%. In contrast to the undoped ferroelectrics, the polarization rotation process is significant and can't be neglected due to the heterogeneity that significantly reduces the anisotropy. As shown in Figure 5E,F, the inclusion of heterogeneities makes the polarizations rotate more easily, especially those within heterogeneities, which results in the large hysteresis and thus the large loss.

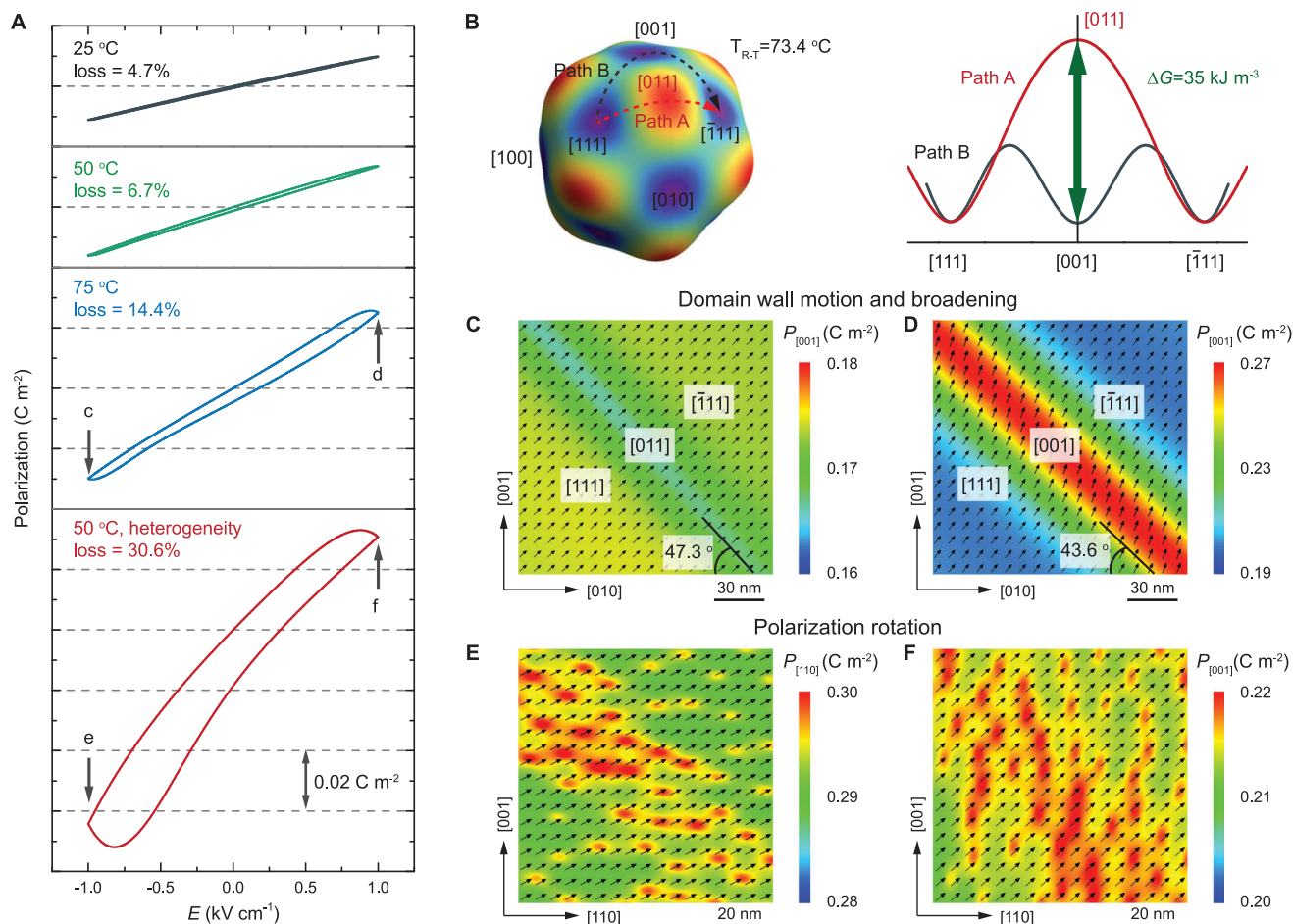


Figure 5. Loss mechanism in PMN-PT by phase-field simulation. A) Simulated P - E hysteresis for the PMN-PT ferroelectrics with and without heterogeneous polar nanoregions at different temperatures, where the poling direction is $[001]$. B) Landau free energy profiles for two paths of PMN-PT at rhombohedral-tetragonal phase transition. C,D) Simulated domain structures corresponding to c and d states of P - E hysteresis at $75\text{ }^\circ\text{C}$ in (A), where domain wall profiles are corresponding to path A and path B in (B), respectively. E,F) Simulated domain structures corresponding to e and f states of P - E hysteresis at $50\text{ }^\circ\text{C}$ with heterogeneity in (A).

3. Conclusion

In summary, based on phenomenological models and phase-field simulations, a synergistic design comprising of local structural heterogeneity and grain orientation/texturing engineering is proposed to enhance piezoelectricity via flattening the energy landscape of polarization. This design is exemplified in Eu^{3+} -doped $\text{Pb}(\text{Mg}_{1/3}\text{Nb}_{2/3})\text{O}_3$ - PbTiO_3 (PMN-PT) textured ceramics that shows the highest small-signal piezoelectric coefficient d_{33} of up to 1950 pC N^{-1} and large-signal piezoelectric coefficient d_{33}^* of $\approx 2100\text{ pm V}^{-1}$. Underlying mechanisms of loss at the domain level is further discussed, which provides a clearer and more comprehensive picture to design high-performance piezoelectric materials. Ultrahigh performance piezoelectric ceramics, as reported here, will enhance the performance of existing devices and open the possibility of developing new actuation and transduction applications. Since the processing of all ceramic materials reported here follows the traditional multi-layer manufacturing process, it is expected that these materials will be equally cost-effective and scalable. Thus, it is expected that these materials

will have tremendous impact on advancing the application domain.

4. Experimental Section

Synthesis of $[001]_{\text{PC}}$ -Textured and Eu^{3+} -Doped PMN-PT Ceramics: A series of $\text{Pb}_{(1-1.5x)}\text{Eu}_x[(\text{Mg}_{1/3}\text{Nb}_{2/3})_{0.72}\text{Ti}_{0.28}]_3\text{O}_3$ matrix powders with $x = 0$ – 0.035 , were synthesized by conventional solid state reaction method. Mixture of PbO (99.9%, Sigma Aldrich, USA), Eu_2O_3 (99.9%, Sigma Aldrich, USA), MgNb_2O_6 (99.9%, Alfa Aesar, USA), and TiO_2 (99.9%, Sigma Aldrich, USA) was ball-milled in ethanol for 24 h using ZrO_2 milling media (Tosoh USA). After drying process, the ball-milled mixture was dried and calcined at $750\text{ }^\circ\text{C}$ for 2 h. Calcined powder was ball-milled again with 1.5 wt% excess PbO for 24 h. The templates for texturing Eu^{3+} doped PMN-PT ceramics are plate-like $[001]_{\text{PC}}$ BaTiO_3 (BT) microcrystals. To synthesize the $[001]_{\text{PC}}$ BT templates, three steps were involved. First, $\text{Bi}_4\text{Ti}_3\text{O}_{12}$ platelets were synthesized by reacting Bi_2O_3 with TiO_2 powders in NaCl and KCl molten salts at $1050\text{ }^\circ\text{C}$ for 1 h. Next, $\text{BaBi}_4\text{Ti}_4\text{O}_{15}$ platelets were synthesized by reacting $\text{Bi}_4\text{Ti}_3\text{O}_{12}$ with TiO_2 and BaCO_3 in BaCl_2/KCl molten salts at $1050\text{ }^\circ\text{C}$ for 3 h. Finally, $[001]_{\text{PC}}$ BT platelets were obtained by topochemical reaction between $\text{BaBi}_4\text{Ti}_4\text{O}_{15}$ and BaCO_3 in NaCl/KCl molten salt at $950\text{ }^\circ\text{C}$ for 3 h. Bi^{3+} in $\text{BaBi}_4\text{Ti}_4\text{O}_{15}$ was substituted by the

Ba²⁺ from BaCO₃, yielding BaTiO₃ template and Bi₂O₃ by-product. The Bi₂O₃ by-product was removed by diluted nitric acid. It should be mentioned here that although a small amount of Bi remains in the lattice of BaTiO₃ template (Bi/Ba is less than 1/20 as shown in Figure S8, Supporting Information), the synthesized BaTiO₃ template has perovskite phase structure (Figure S9, Supporting Information), high aspect ratio morphology (Figure 2C), and good thermal stability (Figure 2C,D) in PMN-PT based matrix, which can be used for fabricating textured ceramics in this study. To fabricate textured ceramics, Eu³⁺ doped PMN-PT matrix powders with organic binder (Ferro 73225, Vista, CA) and toluene/ethanol solvents were mixed by ball-milling to prepare ceramics slurry. Next, various contents of BaTiO₃ templates were added into the slurries under magnetic stirring and the slurries were subsequently casted at the rate of 40 cm min⁻¹ by using doctor blade with height of 200 μm. The dried green tapes were cut, stacked, and laminated at 75 °C under 20 MPa pressure for 15 min. The green samples were heated to 400 °C with a heating rate of 0.3 °C min⁻¹ and held for 2 h to remove organic solvent and binder, and then isostatically pressed under 133 MPa for 1 min. Samples were subsequently sintered at 1175 °C for 10 h in flowing O₂ (0.2 L min⁻¹).

Microstructure Characterization: The crystallographic phase and microstructures of ceramics were characterized using X-ray diffraction (XRD, PANalytical Empyrean) and scanning electron microscopy (FESEM, Apreo) in combination with electron backscatter diffraction (EBSD). The degree of pseudo-cubic [001] texture was determined from the XRD pattern in 2θ range of 20–60° by Lotgering factor method.^[41] The local microstructure of Eu³⁺ doped PMN-PT and interface between textured grain and BT template were observed by FEI Titan³ G2 double aberration-corrected microscope at 300 kV. The STEM images were collected by using a high-angle annular dark field (HAADF) detector which had a collection angle of 52–253 mrad. EDS elemental maps of the sample were collected by using a SuperX EDS system under STEM mode. The TEM sample was prepared by focused ion beam (FIB, FEI Helios 660) lift-out technique. The atomic positions in the HRTEM images were determined by using two-dimensional Gaussian fitting by Atomap software.^[42]

Dielectric and Piezoelectric Property Measurement: The dielectric properties of unpoled and poled samples were measured as a function of temperature by using a multi-frequency LCR meter (Keysight E4980AL). The piezoelectric properties of samples were obtained by resonance and anti-resonance technique using impedance/gain phase analyzer (Keysight E4990A, USA) and d₃₃-meter (YE 2730 A, APC Products, Inc., USA). The polarization versus electric field hysteresis loops and strain versus electric field curves were measured using ferroelectric Tester (Precision Premier II, Radiant Technologies, Inc., USA).

Phase-Field Modeling and Simulations: Phase-field model of polycrystal ferroelectrics is adopted to perform the simulation study of piezoelectric response of PMN-PT ceramics by dopant engineering and texture engineering. In particular, in the phase-field simulations of textured ferroelectric polycrystals, the model of templated grain growth was employed to simulate the grain growth process associated with template seeds, and also the model of template-matrix composites was employed to simulate the piezoelectric properties of textured doped PNM-PT ceramics. The details on the model of templated grain growth can be found in the Supporting Information. In the model of template-matrix composites, the polycrystal grain structure was characterized by the grain rotation matrix field **R**(**r**) while the ferroelectric state was described by the polarization vector field **P**(**r**). The total free energy under externally applied electric field **E**^{ex} is

$$F = \int d^3r \left[f(R_{ij}P_j) + \frac{\beta}{2} \frac{\partial P_i}{\partial r_j} \frac{\partial P_j}{\partial r_i} - E_k^{\text{ex}} P_k \right] + \frac{1}{2} \int \frac{d^3k}{(2\pi)^3} \left[\frac{n_i n_j}{\epsilon_0} \tilde{P}_i \tilde{P}_j^* + K_{ijkl} \tilde{\epsilon}_{ij}^0 \tilde{\epsilon}_{kl}^{0*} \right] \quad (1)$$

where

$$f(\mathbf{P}) = \alpha_1 (P_1^2 + P_2^2 + P_3^2) + \alpha_{11} (P_1^4 + P_2^4 + P_3^4) + \alpha_{12} (P_1^2 P_2^2 + P_2^2 P_3^2 + P_3^2 P_1^2) + \alpha_{111} (P_1^6 + P_2^6 + P_3^6)$$

$$+ \alpha_{112} [P_1^4 (P_2^2 + P_3^2) + P_2^4 (P_3^2 + P_1^2) + P_3^4 (P_1^2 + P_2^2)] + \alpha_{123} P_1^2 P_2^2 P_3^2 \quad (2)$$

is the Landau–Ginzburg–Devonshire (LGD) free energy of the ferroelectric single crystal, and the coefficients of α_i , α_{ij} , and α_{ijk} are functions of r . The operation $R_{ij}P_j$ in $f(R_{ij}P_j)$ in Equation (1) transforms **P**(**r**) from the global system to the local system in each grain. The gradient term in Equation (1) characterizes energy contributions from polarization gradient in domain wall regions. The **k**-space integral terms characterize the long-range electrostatic energy of polarization distribution **P**(**r**) and electrostatic energy of misfit strain distribution $\epsilon^0(\mathbf{r})$. The evolution of the polarization **P**(**r**, *t*) is characterized by the time-dependent Ginzburg–Landau equation

$$\frac{\partial \mathbf{P}(\mathbf{r}, t)}{\partial t} = -L \frac{\delta F}{\delta \mathbf{P}(\mathbf{r}, t)} \quad (3)$$

where *L* is kinetic coefficient. More details on the phase-field models of templated grain growth and template-matrix composites can be found in refs. [43,44].

In this study, the matrix is piezoelectric PMN-30PT which has a rhombohedral phase at room temperature, the templates are made of single-crystalline BaTiO₃, and the local polar nanoregions within the matrix favor the orthorhombic phase. Therefore, the following LGD coefficients are adopted in the phase-field simulations: $\alpha_1 = 0.745(T+160.45) \times 10^5$ m/F, $\alpha_{11} = -0.50 \times 10^8$ m⁵/C²F, $\alpha_{12} = -0.5125 \times 10^8$ m⁵/C²F, $\alpha_{111} = 0.5567 \times 10^9$ m⁹/C⁴F, $\alpha_{112} = 1.333 \times 10^9$ m⁹/C⁴F, $\alpha_{123} = 0.24 \times 10^9$ m⁹/C⁴F for the PMN-30PT matrix;^[45] $\alpha_1 = 3.34(T-381) \times 10^5$ m/F, $\alpha_{11} = 4.69(T-393) \times 10^6 - 2.02 \times 10^8$ m⁵/C²F, $\alpha_{12} = 3.23 \times 10^8$ m⁵/C²F, $\alpha_{111} = -5.52(T-393) \times 10^7 + 2.76 \times 10^9$ m⁹/C⁴F, $\alpha_{112} = 4.47 \times 10^9$ m⁹/C⁴F, $\alpha_{123} = 4.91 \times 10^9$ m⁹/C⁴F for the BaTiO₃ templates;^[46] $\alpha_1 = 2.2(T-560) \times 10^5$ m/F, $\alpha_{11} = -2.67 \times 10^8$ m⁵/C²F, $\alpha_{12} = 2.67 \times 10^8$ m⁵/C²F, $\alpha_{111} = 3.33 \times 10^9$ m⁹/C⁴F, $\alpha_{112} = 3.33 \times 10^8$ m⁹/C⁴F, $\alpha_{123} = 2 \times 10^{10}$ m⁹/C⁴F for the local polar nanoregions.^[12] *T* is the temperature in kelvin. The electrostrictive coefficients are $Q_{11} = 0.055$ m⁴C⁻², $Q_{12} = -0.023$ m⁴C⁻², and $Q_{44} = 0.0315$ m⁴C⁻².

Supporting Information

Supporting Information is available from the Wiley Online Library or from the author.

Acknowledgements

Y.Y., H.L., and S.P. acknowledge the financial support from DARPA through award number HR00111920001. L.G. and Y.W. acknowledge the Extreme Science and Engineering Discovery Environment (XSEDE). Y.Y. and X.L. acknowledge the support through National Science Foundation through the award number DMR-1936432. H.L. acknowledges the financial support from National Science Foundation through award number IIP-1832179. The authors thank Dr. Haiying Wang for FIB sample preparation for TEM. All microscopy work was performed at the Penn State Materials Characterization Laboratory.

Conflict of Interest

The authors declare no conflict of interest.

Data Availability Statement

The data that support the findings of this study are available in the supplementary material of this article.

Keywords

local structural heterogeneity, phase-field simulations, piezoelectric ceramics, texturing

Received: December 9, 2021

Revised: February 3, 2022

Published online:

-
- [1] S. J. Zhang, F. Li, *J. Appl. Phys.* **2012**, *111*, 031301.
- [2] K. Uchino, *Ferroelectric Devices*, 2nd ed., CRC Press, Boca Raton, FL **2009**.
- [3] A. Toprak, O. Tigli, *Appl. Phys. Rev.* **2014**, *1*, 031104.
- [4] M. E. Lines, A. M. Glass, *Principles and Applications of Ferroelectrics and Related Materials*, Clarendon Press, **1979**.
- [5] F. Li, S. J. Zhang, D. Damjanovic, L. Q. Chen, T. R. Shrout, *Adv. Funct. Mater.* **2018**, *28*, 1801504.
- [6] W. F. Liu, X. B. Ren, *Phys. Rev. Lett.* **2009**, *103*, 257602.
- [7] Y. Saito, H. Takao, T. Tani, T. Nonoyama, K. Takatori, T. Homma, T. Nagaya, M. Nakamura, *Nature* **2004**, *432*, 84.
- [8] A. A. Bokov, Z. G. Ye, *J. Mater. Sci.* **2006**, *41*, 31.
- [9] G. H. Haertling, *Ferroelectrics* **1987**, *75*, 25.
- [10] G. H. Haertling, *J. Am. Ceram. Soc.* **1999**, *82*, 797.
- [11] G. A. Samara, *J. Phys.: Condens. Matter* **2003**, *15*, R367.
- [12] F. Li, D. B. Lin, Z. B. Chen, Z. X. Cheng, J. L. Wang, C. C. Li, Z. Xu, Q. W. Huang, X. Z. Liao, L. Q. Chen, T. R. Shrout, S. J. Zhang, *Nat. Mater.* **2018**, *17*, 349.
- [13] F. Li, M. J. Cabral, B. Xu, Z. X. Cheng, E. C. Dickey, J. M. LeBeau, J. L. Wang, J. Luo, S. Taylor, W. Hackenberger, L. Bellaiche, Z. Xu, L. Q. Chen, T. R. Shrout, S. J. Zhang, *Science* **2019**, *364*, 264.
- [14] E. Sun, W. Cao, *Prog. Mater. Sci.* **2014**, *65*, 124.
- [15] Y. K. Yan, Y. U. Wang, S. Priya, *Appl. Phys. Lett.* **2012**, *100*, 192905.
- [16] Y. K. Yan, K. H. Cho, D. Maurya, A. Kumar, S. Kalinin, A. Khachaturyan, S. Priya, *Appl. Phys. Lett.* **2013**, *102*, 042903.
- [17] Y. Yan, J. E. Zhou, D. Maurya, Y. U. Wang, S. Priya, *Nat. Commun.* **2016**, *7*, 13089.
- [18] G. L. Messing, S. Trolier-McKinstry, E. M. Sabolsky, C. Duran, S. Kwon, B. Brahmaroutou, P. Park, H. Yilmaz, P. W. Rehrig, K. B. Eitel, E. Suvaci, M. Seabaugh, K. S. Oh, *Crit. Rev. Solid State Mater. Sci.* **2004**, *29*, 45.
- [19] S. F. Poterala, S. Trolier-McKinstry, R. J. Meyer, G. L. Messing, *J. Appl. Phys.* **2011**, *110*, 014105.
- [20] P. Li, J. W. Zhai, B. Shen, S. J. Zhang, X. L. Li, F. Y. Zhu, X. M. Zhang, *Adv. Mater.* **2018**, *30*, 1705171.
- [21] Y. C. Liu, Y. F. Chang, F. Li, B. Yang, Y. Sun, J. Wu, S. T. Zhang, R. X. Wang, W. W. Cao, *ACS Appl. Mater. Interfaces* **2017**, *9*, 29863.
- [22] Y. F. Chang, B. Watson, M. Fanton, R. J. Meyer, G. L. Messing, *Appl. Phys. Lett.* **2017**, *111*, 232901.
- [23] F. Li, S. Zhang, T. Yang, Z. Xu, N. Zhang, G. Liu, J. Wang, J. Wang, Z. Cheng, Z.-G. Ye, *Nat. Commun.* **2016**, *7*, 13807.
- [24] M. Davis, M. Budimir, D. Damjanovic, N. Setter, *J. Appl. Phys.* **2007**, *101*, 054112.
- [25] F. Li, D. Lin, Z. Chen, Z. Cheng, J. Wang, C. Li, Z. Xu, Q. Huang, X. Liao, L.-Q. Chen, *Nat. Mater.* **2018**, *17*, 349.
- [26] M. Zgonik, P. Bernasconi, M. Duelli, R. Schlessler, P. Gunter, M. H. Garrett, D. Rytz, Y. Zhu, X. Wu, *Phys. Rev. B* **1994**, *50*, 5941.
- [27] F. Li, L. Jin, Z. Xu, S. J. Zhang, *Appl. Phys. Rev.* **2014**, *1*, 011103.
- [28] Y. Yan, K.-H. Cho, S. Priya, *J. Am. Ceram. Soc.* **2011**, *94*, 1784.
- [29] Y. Yan, S. Priya, *Appl. Phys. Lett.* **2015**, *107*, 082909.
- [30] Y. Yan, L. Yang, Y. Zhou, K.-H. Cho, J. S. Heo, S. Priya, *J. Appl. Phys.* **2015**, *118*, 104101.
- [31] D. Berlincourt, in *Ultrasonic Transducer Materials* (Ed: O. E. Mattiat), Springer US, Boston, MA **1971**, p. 63.
- [32] Y. F. Chang, J. Wu, Z. Liu, E. W. Sun, L. J. Liu, Q. W. Kou, F. Li, B. Yang, W. W. Cao, *ACS Appl. Mater. Interfaces* **2020**, *12*, 38415.
- [33] D. Maurya, Y. Zhou, Y. K. Yan, S. Priya, *J. Mater. Chem. C* **2013**, *1*, 2102.
- [34] J. G. Smits, *IEEE Trans. Ultrason. Ferroelectr. Freq. Control* **1976**, *23*, 393.
- [35] G. Liu, S. Zhang, W. Jiang, W. Cao, *Mat. Sci. Eng., R* **2015**, *89*, 1.
- [36] K. Uchino, J. H. Zheng, Y. H. Chen, X. H. Du, J. Ryu, Y. Gao, S. Ural, S. Priya, S. Hirose, *J. Mater. Sci.* **2006**, *41*, 217.
- [37] A. M. Gonzalez, A. Garcia, C. Benavente-Peces, L. Pardo, *Materials* **2016**, *9*, 72.
- [38] Q. H. Guo, L. T. Hou, F. Li, F. Q. Xia, P. B. Wang, H. Hao, H. J. Sun, H. X. Liu, S. J. Zhang, *J. Am. Ceram. Soc.* **2019**, *102*, 7428.
- [39] Y. N. Huang, Y. N. Wang, H. M. Shen, *Phys. Rev. B* **1992**, *46*, 3290.
- [40] D. B. Lin, Z. R. Li, F. Li, S. J. Zhang, *CrystEngComm* **2013**, *15*, 6292.
- [41] F. K. Logtering, *J. Inorg. Nucl. Chem.* **1959**, *9*, 113.
- [42] M. Nord, P. E. Vullum, I. MacLaren, T. Tybell, R. Holmestad, *Adv. Struct. Chem. Imaging* **2017**, *3*, 9.
- [43] J. E. Zhou, Y. K. Yan, S. Priya, Y. U. Wang, *J. Appl. Phys.* **2017**, *121*, 064108.
- [44] J. E. Zhou, Y. K. Yan, S. Priya, Y. U. Wang, *J. Appl. Phys.* **2017**, *121*, 024101.
- [45] H. Zhang, X. Lu, R. Wang, C. Wang, L. Zheng, Z. Liu, C. Yang, R. Zhang, B. Yang, W. Cao, *Phys. Rev. B* **2017**, *96*, 054109.
- [46] A. J. Bell, *J. Appl. Phys.* **2001**, *89*, 3907.